Article

Not peer-reviewed version

Chromium Ferrite Supported into Activated Carbon from Olive Mill Solid Wastes for Photo-Fenton Degradation of Pollutants from Wastewater using LED Irradiation

Malak Hamieh , Sireen Al Khawand , Nabil Tabaja , Khaled Chawraba , Mohammad Hammoud , Sami Tlais , Tayssir Hamieh * , Joumana Toufaily

Posted Date: 4 June 2025

doi: 10.20944/preprints202506.0280.v1

Keywords: Photocatalysis; water treatment; metal ferrites; activated carbon; methylene blue; tetracycline hydrochloride; methyl orange

 doi:10.20944/preprints202506.0280.v1

Article

Chromium Ferrite Supported into Activated Carbon from Olive Mill Solid Wastes for Photo-Fenton Degradation of Pollutants from Wastewater Using LED Irradiation

Malak Hamieh [1,2], Sireen Al Khawand [1,2], Nabil Tabaja [1,2], Khaled Chawraba [1,2], Mohammad Hammoud [3], Sami Tlais [4], Tayssir Hamieh [1,5,6,*] and Joumana Toufaily [1,2]

[1] Laboratory of Applied Studies for Sustainable Development and Renewable Energy (LEADDER), Faculty of Sciences, Doctoral School for Science and Technology (EDST), Lebanese University, Hariri Campus, Hadath P.O. Box 90656, Lebanon

[2] Laboratory of Materials, Catalysis, Environment, and Analytical Methods (MCEMA), Faculty of Sciences, Lebanese University, Hadath P.O. Box 6573, Lebanon

[3] Bahaa and Walid Bassatne Department of Chemical Engineering and Advanced Energy, Faculty of Engineering and Architecture, American University of Beirut, Beirut P.O. Box 11-0236, Lebanon

[4] College of Engineering and Technology, American University of the Middle East, Egaila 54200, Kuwait

[5] Faculty of Science and Engineering, Maastricht University, P.O. Box 616, 6200 MD Maastricht, The Netherlands

[6] Institut de Science des Matériaux de Mulhouse, Université de Haute-Alsace, CNRS, IS2M UMR 7361, F-68100 Mulhouse, France

* Correspondence: t.hamieh@maastrichtuniversity.nl

Abstract: In this study, chromium ferrite (FeCr; $CrFe_2O_4$) nanoparticles supported on activated carbon (AC), obtained from agricultural olive mill solid waste, were synthesized via a simple hydrothermal process. The structural, morphological, optical, and chemical properties of the FeCr/AC composite were characterized using XRD, SEM, EDX, DRS, BET, and FTIR techniques. The FeCr/AC composite was applied as a heterogeneous photo-Fenton catalyst for the degradation of methylene blue (MB) dye in aqueous solution under 25 W visible light LED irradiation. Critical operational factors such as FeCr/AC dosage, pH, MB concentration, and H_2O_2 levels were optimized. Under optimal conditions, 97.56% of MB was removed within 120 minutes of visible light exposure, following pseudo-first-order kinetics. The composite also exhibited high efficiency in degrading methyl orange dye (95%) and tetracycline antibiotic (88%) within 180 minutes, with corresponding first-order rate constants of 0.0225 min^{-1} and 0.0115 min^{-1}, respectively. This study highlights the potential of FeCr/AC for treating water contaminated with dyes and pharmaceuticals, in line with the Sustainable Development Goals (SDGs) for water purification.

Keywords: photocatalysis; water treatment; metal ferrites; activated carbon; methylene blue; tetracycline hydrochloride; methyl orange

1. Introduction

The accumulation of hazardous and non-degradable organic compounds in wastewater, as a result of growing population and increased industrialization, has been recognized as a serious concern in recent years. By 2030, approximately 47% of the global population will face the challenge of clean freshwater scarcity [1]. Global water resources are being contaminated by a variety of contaminants, such as heavy metals, colorants, detergents, drugs, pesticides, and phenols, discharged by industries and municipalities [2]. Among these, dye wastewater is considered the most prevalent form of organic wastewater and has garnered significant researchers' attention. Organic dyes have

 doi:10.20944/preprints202506.0280.v1

been extensively employed in various industrial activities, including printing, plastics, painting, textiles, and food [3]. According to the statistical findings, around 30,000 tons of industrial dyes are released into the ecosystem annually [4,5]. However, many types of dyes are lethal, carcinogenic, and resistant to degradation, resulting in severe environmental pollution and posing irreparable damage to human health and ecosystem [6,7]. Recently, the pursuit of efficient techniques to reduce organic pollutants in wastewater has prompted the investigation of numerous innovative technologies. Over the past decades, conventional methods such as coagulation, electrocoagulation, adsorption, filtration, bioremediation, electrolysis, and chemical oxidation which has been the primary techniques for treating large-scale dye contaminated wastewater [8–13]. The adsorption process is a fast, facile, and economic method for color removal from aquatic bodies [14–16]. However, such method has a major limitation of secondary waste being produced after the contaminants are adsorbed. Additionally, there are environmental concerns related to the reuse of adsorbents for successive batches, the leaching or desorption of pollutants, and the disposal of spent adsorbents. Advanced oxidation processes (AOPs) indeed stand out as a potent method for addressing these challenges [17]. AOPs are used to break down many toxic and biologically persistent organic pollutants in water to acceptable levels, without generating harmful by-products [18]. This method relies on the production of •OH having an oxidation potential of 2.8 V, for the mineralization of pollutants into CO_2, H_2O and inorganic ions [19,20]. Some of the examples of AOP include, photocatalysis, Fenton, photo-Fenton, sono-photo-Fenton, ozonation [21–23]. Heterogeneous photo-Fenton process is considered an economical and environmentally friendly technique for breaking down resistant contaminants due to its fast reaction rate, broad pH range application, and excellent recyclability [24–28].

Currently, spinel ferrite nanoparticles of general molecular formula MFe_2O_4 (M = Ni, Mg, Zn, Co, Cu, Au) are widely valued due to their unique characteristics [29–34]. These include low price, good chemical and thermal stability, strong electrical resistivity, and magnetic anisotropy [35]. In particular, MFe_2O_4 have been widely employed in diverse applications, such as, drug delivery, magnetic resonance image (MRI), cancer diagnosis, electronic devices, adsorption, and photocatalysis [36,37]. As one of its advantages, MFe_2O_4 semiconductors exhibit light response properties, demonstrating efficient photocatalytic activity comparable to the mostly used semiconductors (TiO_2, CdS, ZnO, g-C_3N_4 and SnO_2). Additionally, MFe_2O_4 have lower band gap (2-3 eV) which permit them to absorb light in the visible region [38]. Ferrite nanoparticles still encounter several challenges as they tend to accumulate as a result of Van der Waals forces and magnetic dipolar interactions [39,40]. Also, the leaching of metals in water and the fast electron-hole recombination restrict their relevance in photocatalytic applications. Thus, the aforementioned issues can be mitigated by loading metal ferrites into suitable support materials.

Activated carbon (AC) is commonly employed in water purification either as an adsorbent or a carrier [41,42]. Its high surface area and porosity allow AC to effectively, quickly, and completely capture targeted contaminants, offering a notable advantage over other supports in playing this role [43]. The sustained high cost of commercial AC limits its application in large industrial scale [44]. Olive mill agricultural solid wastes (OMSW) could be valorized into low cost AC as one of the eco-friendly methods used to reduce their negative environmental impacts. Around 20 million tons of OMSW are produced every year [45]. In photocatalysis application, AC is extensively used as a support material for the deposition of metals and metal oxides. Recent research has shown that the combination of AC with suitable semiconductors, improved the efficacy in catalytic oxidation and acts as a highly stable photocatalyst for decomposing numerous contaminants [46,47]. Additionally, the loading of semiconductors on AC resulted in band gap reduction, increased solar energy collection, improved pollutant adsorption and decreased electron-hole recombination [48,49]. Therefore, it is feasible to enhance the photo-Fenton activity of metal ferrites by coupling them with AC.

In the present work, a composite mixture FeCr/AC was prepared by hydrothermal method. The primary objective of this research is to reduce the leaching rate associated with the use of iron oxide in aqueous solutions while simultaneously decreasing the band gap, which enhances photocatalytic

 doi:10.20944/preprints202506.0280.v1

activity [50,51]. Additionally, chromium ferrite exhibits moderate hydrogen peroxide scavenger properties, further contributing to its potential in various applications [52]. On the contrary, the high surface area of AC plays a crucial role in improving catalytic activity. The production of AC with desirable physicochemical properties from agricultural biomass waste aligns with the ongoing efforts in sustainable development and the promotion of green energy within the scientific community. AC from olive mill solid waste was prepared by chemical impregnation with zinc chloride. The synthesized materials were characterized by different techniques (XRD, BET, SEM-EDX, FT-IR, UV-Vis) to study their physicochemical properties. The FeCr/AC composite was used to study the photo-Fenton degradation of different types of model pollutants. The photo-Fenton performance of MB was evaluated by modifying several factors such as contact time, catalyst loading, dye concentration, and pH on the degradation of MB. Additionally, the innovative design of our composite promotes higher reusability and stability, addressing key challenges in photocatalytic applications. The degradation performance was further tested using methyl orange (MO) and the tetracycline antibiotic to validate the composite's versatility across different pollutant classes.

2. Materials and Methods

2.1. Chemicals

All reagents utilized in this study were of analytical grade and employed without any additional purification. Zinc chloride ($ZnCl_2$), iron nitrate nonahydrate ($Fe(NO_3)_3.9H_2O$), chromium nitrate nonahydrate ($Cr(NO_3)_3.9H_2O$), ammonia (NH_3, 25% w/w), hydrochloric acid (37% HCl), sodium hydroxide (NaOH), hydrogen peroxide (H_2O_2, 35% w/w) Methylene blue ($C_{16}H_{18}N_3SCl$, MW:373.88 g/mole), methyl orange ($C_{14}H_{14}N_3NaO_3S$, MW:327.33 g/mole) and tetracycline hydrochloride ($C_{22}H_{24}N_2O_8{\cdot}HCl$, MW: 480.90) were all procured from Sigma-Aldrich.

2.2. Preparation of Activated Carbon Support

The collected olive-processing residues were initially washed using deionized water and then crushed and sieved to obtain uniform particle size. The resulting particles were impregnated with $ZnCl_2$ solution (impregnation ratio of $ZnCl_2$ to OMSW = 2:1) for 24 hours at ambient temperature. Following impregnation, the sample was oven-dried at 110 ºC for 24 h. The dried mixture was transferred to a sealed crucible and subjected to thermal treatment in a programmable muffle furnace at 500 ºC for 2 h with a heating rate of 5 ºC min^{-1}. The obtained AC was then cooled and washed with 0.1 M HCl and distilled water to eliminate any residual chlorides and mineral matter. Finally, the AC was dried again at 110 ºC and stored for further use.

2.3. Preparation of Composite Mixture (FeCr/AC)

Chromium ferrite supported on activated carbon (AC), derived from OMSW, was prepared using the hydrothermal method. First a known mass of metal nitrate solutions, $Fe(NO_3)_3{\cdot}9H_2O$ and $Cr(NO_3)_3{\cdot}9H_2O$, were each dissolved in 10 mL distilled water in two separate beakers to achieve final percentages of 8% iron and 4% chromium in the final prepared catalyst. The two solutions were then mixed together, after which one gram AC was added to them. Following this, the suspension was sonicated for 1 h to obtain a uniform suspension and to ensure the proper dispersion of iron and chromium precursors on the AC surface. Then, an ammonia solution (25% w/w) was added into the suspension until the pH reached 10. The resulting solid was collected through filtration, thoroughly rinsed with deionized water, and then left to dry overnight at 110 °C. Subsequently, the dried powders were subjected to calcination at 500 °C for 2 hours using a heating rate of 5 °C per minute.

2.4. Characterization Techniques

Various analytical tools were employed to characterize the synthesized materials. The crystal structure and phase composition of both AC and FeCr/AC composites were examined via X-ray

 doi:10.20944/preprints202506.0280.v1

diffraction (XRD) using a Bruker D8 Advance diffractometer equipped with a Cu Kα radiation source (λ = 1.5418 Å), operated at 40 kV and 40 mA, and scanned over a 2θ range of 10°–60°. The textural properties, including surface area and porosity, were investigated by nitrogen adsorption-desorption measurements at 77 K using a Micromeritics Gemini VII 2390p analyzer. Before analysis, the samples were degassed under vacuum at 120 °C overnight. The specific surface area (S_{BET}) was derived using the BET method over a relative pressure range of 0.01–0.1. Pore distribution was determined by the Barrett-Joyner-Halenda (BJH) method applied to the desorption curve, while micropore volume was obtained using the t-plot technique.

To assess the surface morphology and elemental content, scanning electron microscopy (SEM) analysis was conducted using a Tescan MIRA3 microscope fitted with an EDX detector. A small amount of catalyst powder was affixed to a carbon-coated aluminum stub and coated with approximately 5 nm of gold by sputtering. Functional groups present on the AC and FeCr/AC surfaces were identified using FTIR spectroscopy (Thermo Nicolet Summit-LITE), scanning in the 400–4000 cm^{-1} range at a resolution of 4 cm^{-1}. The optical properties and band gap of FeCr/AC were assessed through diffuse reflectance spectroscopy (DRS) with a Perkin Elmer UV-Vis-NIR spectrophotometer (Lambda 1050+ model).

2.5. Process for Photo-Fenton Degradation Experiment

The photocatalytic degradation experiment was conducted in a 250 mL beaker under visible light using a 25 W white LED lamp. Different pollutants including cationic dye (methylene blue, MB), anionic dye (methyl orange, MO) and pharmaceutical (tetracycline hydrochloride) were taken as model pollutants. For the degradation of MB pollutant, varying doses of FeCr/AC were suspended in 100 mL of MB solution with an initial concentration of 20 ppm. The suspension was stirred in the dark for 30 min before irradiation to achieve an equilibrium state between the pollutant and catalyst. Next, the lamp was turned on and 0.25 mL H_2O_2 was introduced into the beaker. Samples were then withdrawn at different time intervals (t = 0 to t = 180 minutes). These samples were filtered using a 0.45 μm syringe filter. The concentration of residual pollutants in the filtered solution was recorded using a UV-visible spectrophotometer by measuring the absorbance at maximum wavelengths of 664, 464, and 365 nm for MB, MO, and TCH, respectively. The degradation efficiency was computed using **Equation (1)**.

$$Degradation\ efficiency\ (\%) = \frac{(C_0 - C_t)}{C_0} \times 100 \quad (1)$$

where, C_0: initial pollutant concentration (mg L^{-1}) and C_t: pollutant concentration at time t (mg L^{-1}).

3. Results

3.1. X-Ray Diffraction

Figure 1 displays the wide-angle XRD patterns of the AC support and the FeCr/AC composite. For AC, a broad peak appears within the 2θ range of 20–30°, which corresponds to the (002) reflection plane typically associated with hexagonal graphitic carbon structures. [53]. FeCr/AC showed sharp and intense peaks at 2θ angles of 30º, 35.5º, 43º, 53.5º,57º, 62.5º, and 74º, which can be indexed to planes (220), (311), (400), (422), (511), (440), and (533), respectively [54]. These peaks are in good agreement with the cubic spinel structure of metal ferrites with space group Fd-3m according to JCPDS card no.10-0325 [55]. No other impurities were detected in the XRD pattern, which indicates the high purity of the synthesized material. Therefore, $CrFe_2O_4$ nanoparticles are effectively incorporated into AC.

 doi:10.20944/preprints202506.0280.v1

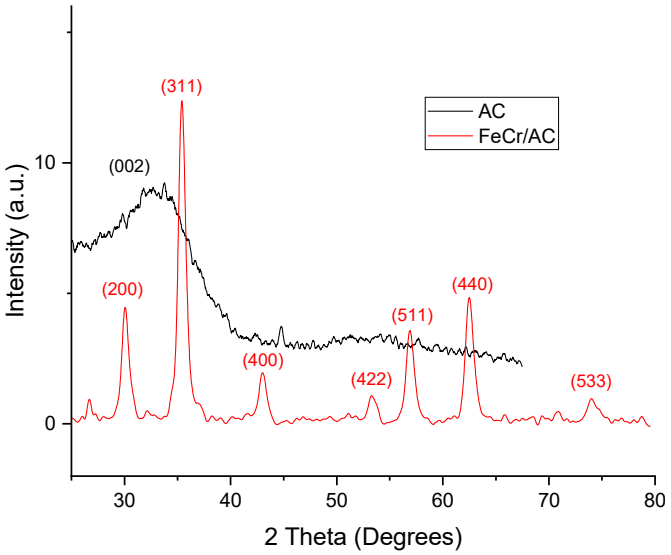

Figure 1. Wide angle XRD of AC and FeCr/AC.

3.2. Brunaeur-Emmet-Teller (BET)

The surface area and pore structure of the pure AC support and FeCr/AC were assessed by nitrogen adsorption-desorption isotherms at 77 K. The isotherms are displayed in **Figure 2**. The adsorption isotherm of AC exhibited a type I isotherm, typical for microporous materials. This is accompanied by a hysteresis loop of type H4 in the relative pressure range of 0.4-0.8 P/P_0. The prominent hysteresis loop, which is a property of mesoporous materials, is caused by capillary condensation in slit-shaped pores. Conversely, the sorption isotherm of modified FeCr/AC revealed type IV isotherm associated with H1 hysteresis loop, typical for mesoporous materials [56].

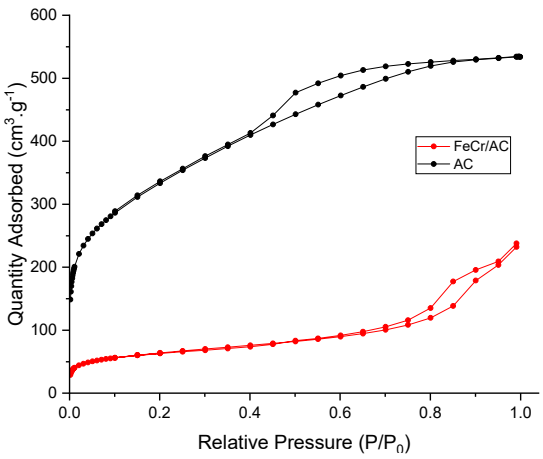

Figure 2. N_2 adsorption-desorption isotherm of AC and FeCr/AC.

The textural parameters, including BET surface area (S_{BET}), total pore volume (V_P), pore diameter (D_P), and micropore volume ($V_{\mu p}$) of the prepared AC and FeCr/AC are listed in **Table 1**. The AC exhibited a high S_{BET} 1148 $m^2\ g^{-1}$ and a V_p of 0.6 $cm^3\ g^{-1}$. After deposition of Cr and Fe, there was a significant reduction in the S_{BET} and V_p to 222 $m^2\ g^{-1}$ and 0.3 $cm^3\ g^{-1}$, respectively. The reduction in surface area after metal deposition suggests that the nanoparticles are well incorporated within AC pores.

Table 1. Textural characteristics of AC and FeCr/AC measured by N_2 sorption at 77K.

Sample	S_{BET} ($m^2\ g^{-1}$)	V_p ($cm^3\ g^{-1}$)	D_{pore} (nm)	$V_{\mu p}$ ($cm^3\ g^{-1}$)
Pure AC	1148	0.6	3.2	0.055

 doi:10.20944/preprints202506.0280.v1

FeCr/AC	222	0.32	9.7	0.025

3.3. Fourier Transform Infrared (FT-IR)

Figure 3 presents the FTIR spectra of AC and FeCr/AC. For both spectra there existed a wide and large band at 3365 cm^{-1}, which refers to the stretching vibration band of OH in carbonyl, hydroxyl, or adsorbed H_2O molecules. The intensity of this band decreased following the incorporation of metals in the FeCr/AC spectrum. The stretching vibration band of C=C in benzene ring is confirmed by the peak observed at 1570 cm^{-1} in the spectrum of AC [57]. While, in FeCr/AC, a band was detected at 1620 cm^{-1}, which can be assigned to the asymmetric stretching vibration of C=O [58] or the bending vibration of H_2O [59]. The absorption band at 946 cm^{-1} in FeCr/AC confirmed the presence of aromatic group [60]. Additionally, the band observed at 2970 cm^{-1} corresponded to the symmetric stretching vibration of C-H [61]. A sharp and intense absorption band appeared at 570 cm^{-1} in the spectrum of FeCr/AC, which was absent in AC spectrum. This newly formed band can be attributed to the stretching vibration of M-O at the tetrahedral sites [62].

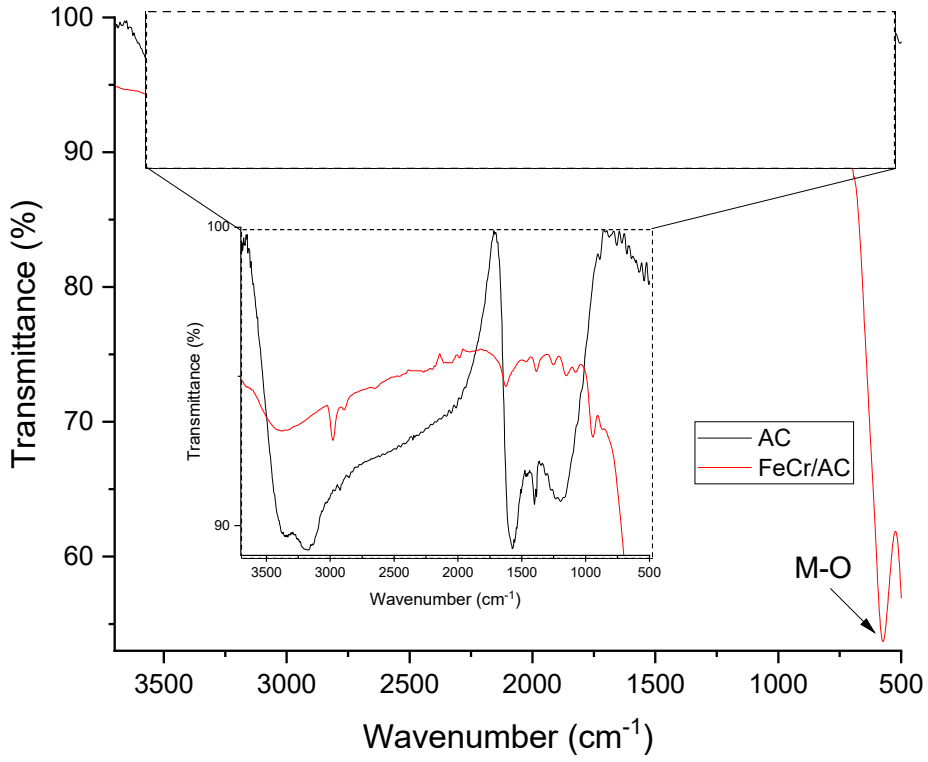

Figure 3. FT-IR spectra of AC and FeCr/AC.

3.4. Scanning Electron Microscope (SEM)

The surface morphology and elemental distribution of the synthesized samples were analyzed through SEM imaging combined with EDX spectroscopy, as presented in **Figure 4**. The SEM micrograph of AC revealed an irregular, heterogeneous, rough surface full of cavities and voids. In **Figure 4b**, a rigid surface with some stacks was also observed, indicating that chromium ferrite nanoparticles are dispersed throughout the AC surface.

For further analysis of elemental composition, the relevant regions of AC and FeCr/AC are detected by EDS mapping. As shown in **Figure 4c**, AC comprises mainly two components (carbon and oxygen) with relative abundances 89.16 and 10.84 wt.%, respectively. However, after modification with chromium ferrite, new peaks for Fe and Cr are observed in **Figure 4d** with relative abundances of 7.79 and 3.9 wt.%, respectively. These findings confirm the successful incorporation of Fe and Cr into the AC material.

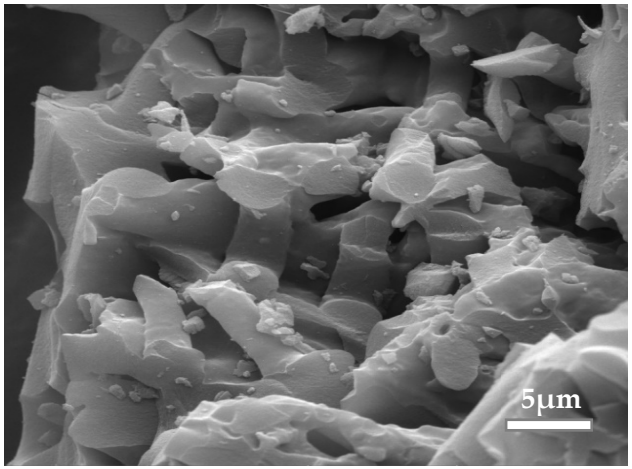

(a)

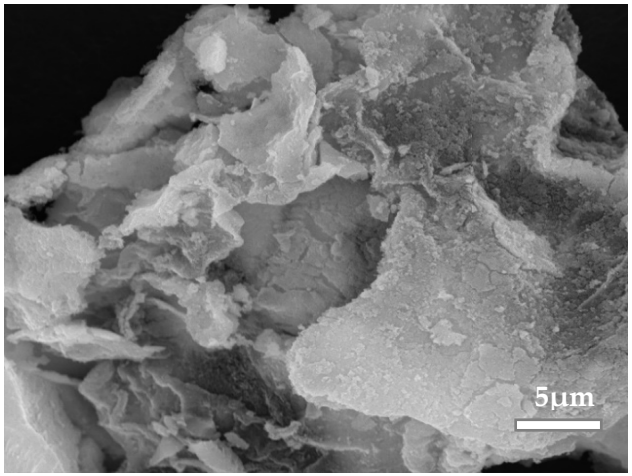

(b)

Elements	Weight %
C	89.16
O	10.84

(c)

Elements	Weight %
C	53.04
O	36.6
Fe	7.79
Cr	2.58

(d)

Figure 4. SEM images and EDX results for AC (a,c) and FeCr (b,d) respectively.

 doi:10.20944/preprints202506.0280.v1

3.5. UV-Vis Spectroscopy

In order to evaluate the optical characteristics and estimate the band gap of the synthesized materials, DRS spectra were recorded, and the findings are illustrated in **Figure 5a**. Spinel ferrite nanoparticles exhibit light absorption within the visible range due to electrons transition from the O-2p level to the Fe-3d level [63]. The optical behavior evident in the DRS data for ferrites is attributed to electron excitation occurring from the valence band (VB) to the conduction band (CB). This excitation energy is directly linked to the ferrite band gap. In general, the Kubelka–Munk method is utilized with DRS data to compute the band gap (**Equation (2).**

$$F(R) = \alpha = \frac{(1-R)^2}{2R} \quad (2)$$

Here, F(R) denotes the Kubelka–Munk function, α refers to the absorption coefficient, and R represents the reflectance.

The Tauc plot equation is represented as follows in **Equation (3)**:

$$(F(R)hv)^{\frac{1}{n}} = A(hv - E_{BG}) \quad (3)$$

In this relation, h is Planck's constant, A is a proportionality factor, v is the frequency of incident photons, and E_{BG} indicates the band gap energy. The exponent n varies based on the type of electronic transition. Depending on the type of transition, n can be 2 for indirect or ½ for direct transitions. As reported in literature, spinel ferrites have a direct band gap [64]. Therefore, in our case n is equal to ½. The Tauc plot of FeCr/AC is shown in **Figure 5b**. As revealed, the band gap energy for FeCr/AC is 1.9 eV. These findings reveal the narrow band gap of these nanoparticles, emphasizing their potential as an efficient visible-light photocatalyst.

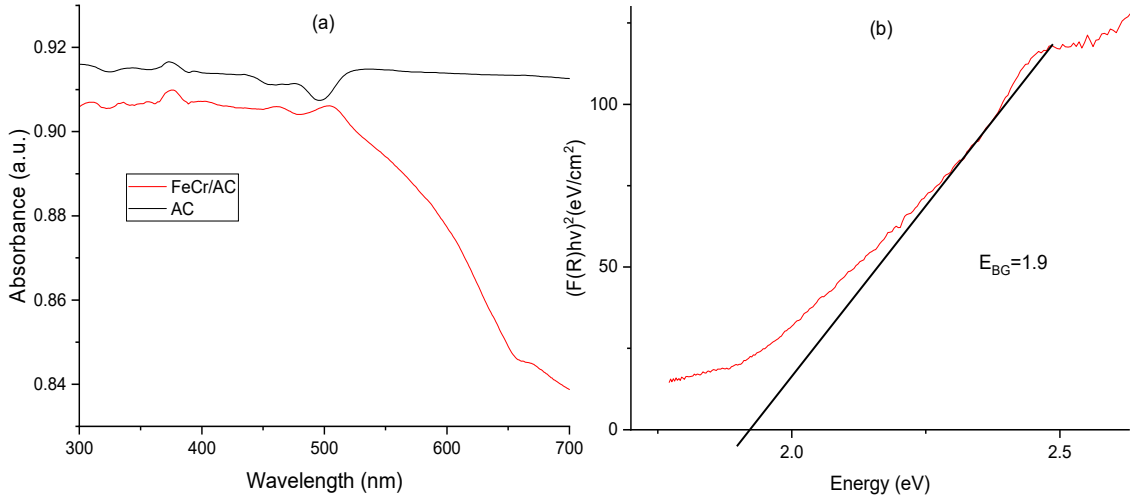

Figure 5. UV-Vis absorption spectra of AC and FeCr/AC (a) and Tauc plot of FeCr/AC (b).

3.6. Photo-Fenton Catalytic Activity of FeCr/AC

Several experimental conditions were tested to compare the decolorization efficiency of MB, and the results are presented in **Figure 6**. These conditions included visible light only, FeCr/AC with visible light, FeCr/AC with H_2O_2 and visible light, and FeCr/AC in the dark. The blank experiment, conducted under visible light irradiation and in the absence of FeCr/AC catalyst and H_2O_2, revealed only 1.6% MB degradation after 120 min, indicating that the photolysis reaction was negligible. Prior to illumination, a dark experiment was performed for 180 min to study the adsorption of MB onto FeCr/AC. Equilibrium between adsorption and desorption was achieved within 30 minutes, resulting in a 25% removal of MB attributed to the adsorption process. Interestingly, the results revealed a complete decolorization of MB (97.56%) after 120 min when FeCr/AC was irradiated with 25W LED lamp in the presence of H_2O_2. This result is significantly higher than that obtained using FeCr/AC alone (35%) in the presence of visible light without adding H_2O_2. Thus, H_2O_2 plays a pivotal function

 doi:10.20944/preprints202506.0280.v1

in the degradation mechanism of MB and facilitates the oxidation reactions in photocatalytic activities [65]. The aforementioned findings showed that the combination of FeCr/AC, H_2O_2, and visible light are necessary for effective photo-Fenton degradation of MB dye.

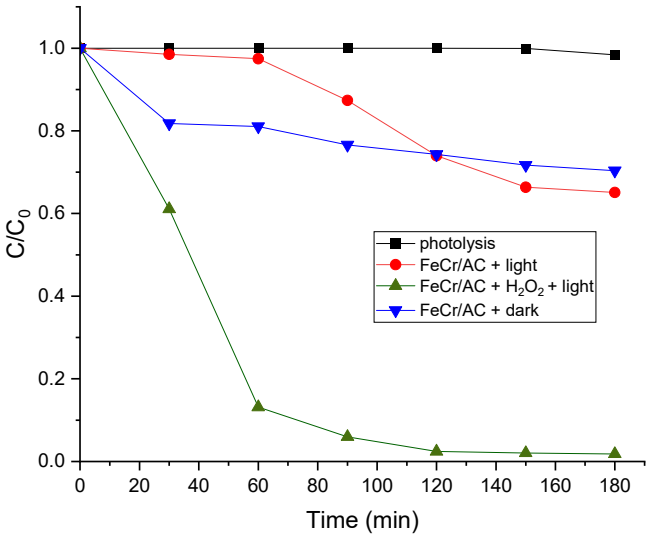

Figure 6. MB removal efficiency under various experimental conditions ([MB]=20 mg L^{-1}, 250 ppm FeCr/AC, 0.25 mL H_2O_2 and pH=5.47).

3.7. Impact of Catalyst Amount on MB Degradation

The influence of FeCr/AC dosage on MB degradation was investigated using a varying FeCr/AC quantity of 125, 250, and 400 ppm, at fixed MB concentration of 20 ppm, 0.25 mL H_2O_2 (35%), and a near-neutral pH of 6.47 (**Figure 7)**. The results revealed an improvement in MB degradation from 54.2 % to 86.8% as the catalyst amount increased from 125 ppm to 250 ppm at 60 min under LED irradiation. This enhancement can be attributed to the increased availability of active sites on the FeCr/AC surface, which improves its light-harvesting capability. As more photons are absorbed, more charge carriers are generated, resulting in an increase in the number of hydroxyl radicals formed and, consequently, improved the degradation of MB. However, there was almost no improvement in the degradation of MB as the catalyst amount exceeded 250 ppm, possibly due to agglomeration of nanoparticles at high catalyst doses. Thus, in our study, the optimum dosage of FeCr is determined to be 250 ppm.

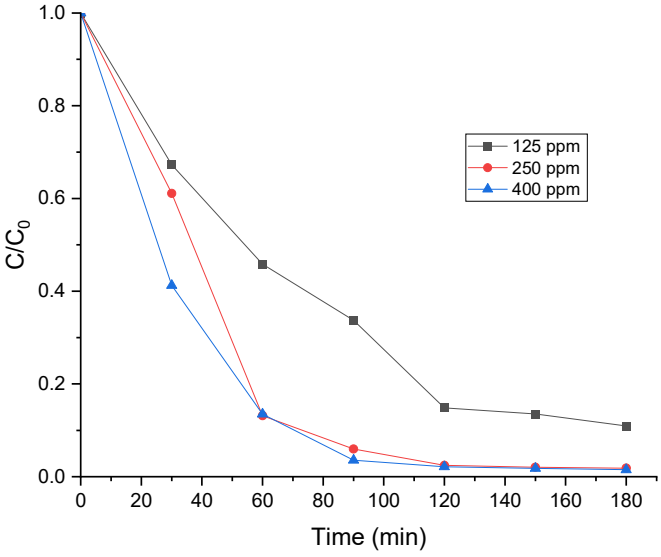

Figure 7. Effect of FeCr/AC mass on the degradation of MB.

 doi:10.20944/preprints202506.0280.v1

3.8. Impact of Initial MB Concentration

The effect of the starting dye concentration on MB degradation was investigated by varying MB levels between 10 and 100 ppm, with a fixed catalyst amount of 250 ppm, 0.25 mL H_2O_2, and a near-neutral pH of 6.47. The degradation of MB is reduced from 92% to 43.6% as the MB concentration rose from 10 ppm to 100 ppm. This reduction could be ascribed to the increase in the number of MB molecules to be degraded which hinders a significant portion of light from reaching the FeCr/AC surface (**Figure 8)**. This reduction in light exposure decreases the production of hydroxyl radicals responsible for degrading MB [66], Furthermore, the intermediates produced during MB decomposition compete with MB molecules for the available catalyst surface [67].

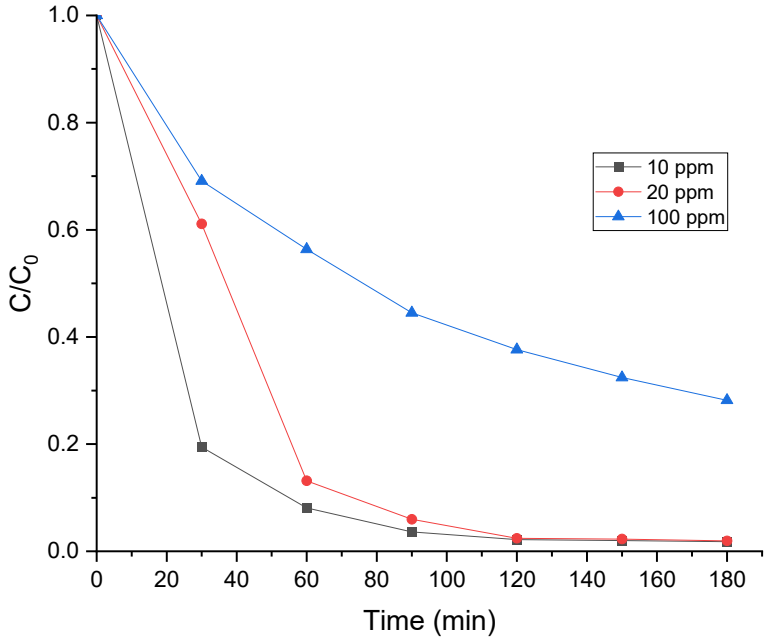

Figure 8. Effect of initial MB concentration on its degradation efficiency using by FeCr/AC.

3.9. Impact of Initial pH

The influence of solution pH on the degradation of MB by FeCr/AC was examined using three distinct pH values (3, 6.47 and 10) with 250 ppm FeCr/AC, 20 ppm MB, and 0.25 mL H_2O_2. The results are represented in **Figure 9**. The degradation of MB was highest at neutral pH and reached 87% in 60 min, indicating that neutral conditions are favorable for the photo-Fenton degradation of MB. However, a decline in MB degradation was observed under acidic and basic conditions, at 29% and 50%, respectively. The reduction in MB degradation at acidic pH was expected due to the electrostatic repulsion between MB cationic dye and surface of FeCr/AC. In contrast, in alkaline conditions, despite the negatively charged environment, the degradation of MB was reduced to 50%. This reduction is attributed to production of weak oxidant ferryl ions (FeO^{2+}) which are formed at pH > 5 according to **Equation (4)** [68]. Additionally, in a basic medium, hydrogen peroxide oxidant is unstable and its degradation produces water and oxygen (**Equation 5**). In this study, the optimum pH was determined to be 6.47.

$$Fe^{2+} + H_2O_2 \rightarrow FeO^{2+} + H_2O \quad (4)$$

$$2H_2O_2 \rightarrow 2H_2O + O_2 \quad (5)$$

 doi:10.20944/preprints202506.0280.v1

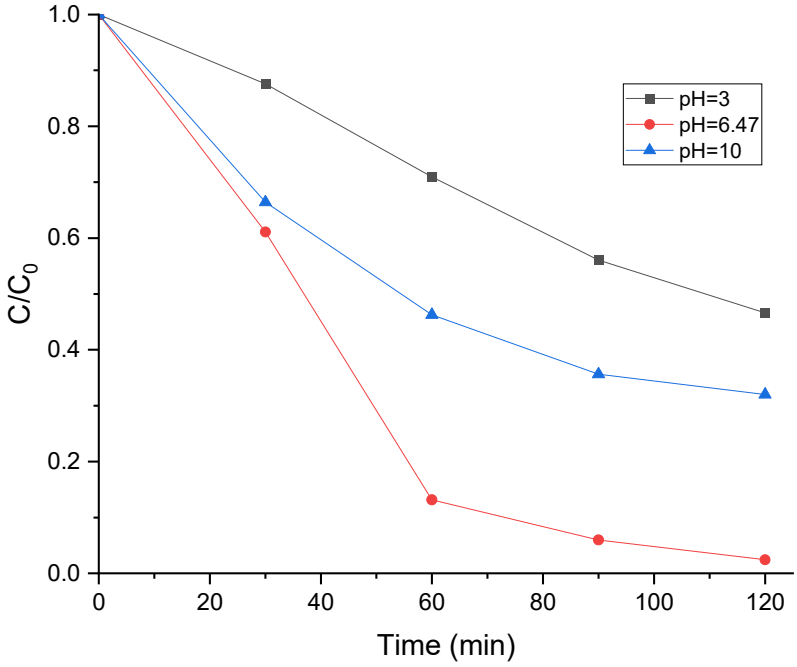

Figure 9. Effect of pH on the degradation efficiency of MB using FeCr/AC.

3.10. Impact of Oxidant Dosage on MB Degradation

In the photo-Fenton oxidation process, H_2O_2 plays a key role in generating hydroxyl radicals, which participate in the mineralization of MB dyes. The impact of H_2O_2 amount was evaluated using different concentrations of H_2O_2 ranging from 0.25 mL to 1.0 mL at 250 ppm FeCr/AC, MB concentration of 20 ppm, and neutral pH. As shown in **Figure 10**, almost complete degradation of MB (97%) was attained when the H_2O_2 concentration was 0.25 mL. However, the degradation decreased gradually from 97% to 86.6% as the concentration of H_2O_2 increased to 1 mL. This reduction is due to the formation of hydroperoxyl radicals ($HO_2 \cdot$) at excess concentrations, which act as scavengers of hydroxyl radicals (**Equation 6**) [69]. Therefore, in our study, the addition of only 0.25 mL of H_2O_2 was sufficient to optimize the degradation of MB.

$$H_2O_2 + \cdot OH \rightarrow H_2O + \cdot OOH \quad (6)$$

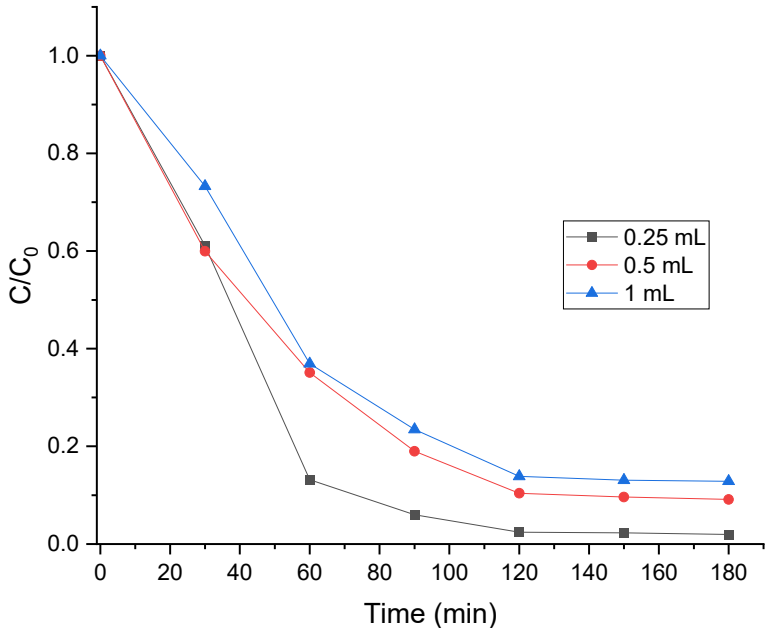

Figure 10. Influence of H_2O_2 dosage on the degradation performance of MB.

 doi:10.20944/preprints202506.0280.v1

3.11. Kinetic Study of MB

The degradation rate of MB can be evaluated using kinetic parameters. To ascertain the kinetics of the degradation of MB, the experiment was performed using 250 ppm FeCr/AC, pH of 6.47, and time interval up to 180 min under visible LED light. The degradation kinetics of MB at different concentrations (10, 20, and 100 ppm) were studied by plotting of ln (C_0/C_t) versus time (min). The rate constant (k_{app}) was determined from the slope of the linear graph (**Equation 7)**. **Table 2** presents the values of the decomposition rate constant (k) and the half-life time ($t_{1/2}$) for the different initial concentrations of MB (**Equation 8)**. As shown in **Table 2**, the Langmuir-Hinshelwood pseudo-first-order kinetic model fits the experimental data well, with $R^2 > 0.97$. The calculated rate constants for different concentrations of MB were 0.0297 min^{-1}, 0.0258 min^{-1}, and 0.0077 min^{-1} for 10 ppm, 20 ppm, and 100 ppm concentrations of MB, respectively. The reaction rate constant reduced from 0.0297 min^{-1} to 0.0077 min^{-1} with increasing MB concentration from 10 ppm to 100 ppm. At elevated concentrations, the increased amount of intermediate products restricts the availability of active hydroxyl radicals, causing a decrease in the degradation rate constant. Conversely, the half-life of MB increased from 23.33 min^{-1} to 89.78 min^{-1} as the concentration of MB increased from 10 ppm to 100 ppm.

$$\ln\left(\frac{C_0}{C_t}\right) = k_{app}t \quad (7)$$

$$t_{1/2} = \frac{ln2}{k_{app}} \quad (8)$$

where C_o: MB initial concentration (mg L^{-1}), C_t: final concentration (mg L^{-1}), k_{app}: first order rate constant (min^{-1}), t: reaction time (min), and $t_{1/2}$: half-life time (min).

Table 2. First-order kinetic parameters for MB degradation using FeCr/AC under different initial concentrations.

Concentrations (ppm)	k (min^{-1})	R^2	$t_{1/2}$ (min)
10	0.0297	0.9785	23.33
20	0.0258	0.9739	26.9
100	0.0077	0.9873	89.78

3.12. FeCr/AC Recyclability and Leaching Test

The reusability of the catalysts is a crucial requirement for industrial applications. To assess the reusability of FeCr/AC under visible light, the catalyst was tested over three consecutive cycles. Following each cycle, the catalyst was recovered from the MB solution, washed with deionized water, and then dried at 100 °C prior to its reuse in subsequent reactions. The photocatalytic efficiency of FeCr/AC remained high, starting at 98% in cycle 1, achieving 92.76% in cycle 2, and maintaining a robust 85.41% in cycle 3. These results validate the reusability and durability of the prepared photocatalyst nanocomposite. Moreover, the leaching of Fe in the solution as detected by atomic absorption spectroscopy was very low (0.1 ppm), which is below the acceptable level. The level of Cr leaching was below the detection limit.

3.13. Possible Mechanism for MB Degradation by FeCr/AC

When chromium ferrite nanoparticles supported on AC absorb visible light, electron-hole pairs are generated. The electrons (e^-) in the valence band (VB) of $CrFe_2O_4$/AC are promoted to the conduction band (CB), leaving behind holes (h^+) in the VB (**Equation 9**). The e^- produced in the CB can interact with the absorbed O_2 molecules, leading to the formation of superoxide anions ($O_2^{-\bullet}$) (**Equation 10**). These anions can directly degrade MB molecules or react with H_2O_2 to produce hydroxyl radicals (OH•) (**Equation 11**). On the contrary, the h^+ in the VB may react with H_2O

 doi:10.20944/preprints202506.0280.v1

molecules to form OH• (**Equation 12**). These radicals are potent oxidizers responsible for MB degradation (**Equation 13**) [70].

$$CrFe_2O_4/AC + \hbar v \rightarrow e_{CB}^- + \hbar_{VB}^+ \quad (9)$$

$$e_{CB}^- + O_2 \rightarrow O_2^{-\cdot} \quad (10)$$

$$H_2O_2 + O_2^{-\cdot} \rightarrow OH\cdot + OH^- + O_2 \quad (11)$$

$$\hbar_{VB}^+ + H_2O \rightarrow OH\cdot + H^+ \quad (12)$$

$$MB\ dye + OH\cdot\ or\ O_2^{-\cdot} \rightarrow CO_2 + H_2O + mineralization\ products \quad (13)$$

3.14. Degradation of MO and TCH

The photocatalytic performance of FeCr/AC under visible LED irradiation is investigated for the degradation of MO and TC using 250 ppm FeCr/AC, 20 ppm MO, 20 ppm TCH, and 0.5 mL H_2O_2, without modifying the solution pH (5.47 for MO and 4.4 for TCH). **Figure 11** presents the degradation results for both pollutants. Dark experiments were also performed for 180 min to assess the adsorption of MO and TCH. The results revealed no adsorption of MO and around 17% adsorption of TCH. According to **Figure 11**, maximum removal rates of 88% for MO and 97% for TC were observed.

Langmuir-Hinshelwood first-order kinetic model is suitable to fit the degradation of MO and TCH. The first-order kinetic parameters k, R^2, and $t_{1/2}$ for MO and TCH are mentioned in **Table 3**. The obtained k_1 values for TCH and MO were 0.0225 min^{-1} and 0.0115 min^{-1}, respectively.

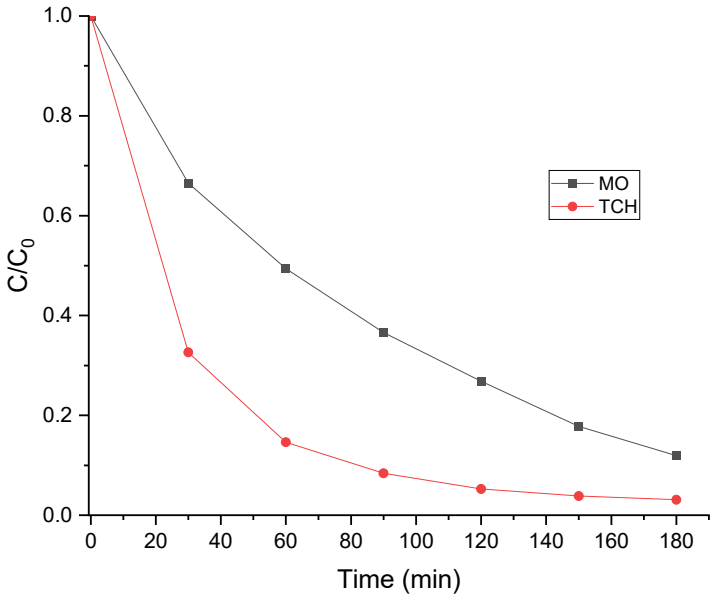

Figure 11. Degradation of MO and TCH.

Table 3. First-order kinetic parameters for MO and TCH.

Pollutant	First-order kinetic		
	k (min^{-1})	R^2	$t_{1/2}$ (min)
MO	0.0115	0.9988	60.27
TCH	0.0225	0.9731	30.8

4. Conclusions

FeCr/AC composite was prepared by hydrothermal synthesis process and used to study the degradation of MB dye and different pollutants (MO and TCH) using heterogeneous photo-Fenton process under visible 25 W LED illumination. The physicochemical characteristics of FeCr/AC were

 doi:10.20944/preprints202506.0280.v1

investigated using techniques, including XRD, BET, SEM, EDX, FT-IR, and DRS. The characterization results confirmed the successful incorporation of chromium ferrite nanoparticles into AC support. Moreover, the band gap of FeCr/AC, determined from DRS spectra, was 1.9 eV demonstrating its efficiency in visible light photocatalytic applications. The prepared FeCr/AC catalyst exhibited high efficacy in the decolorization of MB, achieving a 97% removal efficiency within 120 min in a neutral environment using only 0.25 mL H_2O_2 under visible LED illumination. The degradation kinetics of MB using FeCr/AC followed a pseudo-first-order model, yielding a rate constant of 0.0258 min^{-1} at an initial concentration of 20 ppm. Furthermore, FeCr/AC demonstrated notable reusability and stability, with only a minor reduction in degradation performance observed after three consecutive cycles. Additionally, FeCr/AC showed high removal rates for MO and TCH 88% and 97%, respectively within 180 min under the specified reaction conditions: 250 ppm FeCr, 0.5 mL H_2O_2, and an unmodified pH. The corresponding rate constants of MO and TCH were 0.0115 and 0.0225 min^{-1}, respectively. Therefore, the prepared FeCr/AC catalyst shows promise for large-scale application in the effective treatment of contaminated water containing diverse pollutants.

Author Contributions: "Conceptualization, all authors; methodology, all authors; software, M.H.; validation, all authors; formal analysis, all authors; investigation, M.H., S.A., and K.C.; resources, J.T. and M.H.; data curation, M.H. and J.T.; writing—original draft preparation, all authors; writing—review and editing, M.H., J.T., and T.H.; visualization, All authors; supervision, J.T.; project administration, J.T.; funding acquisition, J.T. All authors have read and agreed to the published version of the manuscript."

Funding: "This research received no external funding".

Institutional Review Board Statement: "Not applicable".

Informed Consent Statement: "Not applicable".

Data Availability Statement: All data generated or analyzed during this study are included in this published article.

Acknowledgments:

Conflicts of Interest: "The authors declare no conflicts of interest."

References

1. World Economic Forum (2020). *5 lessons for the future of water*. Available at: https://www.weforum.org/agenda/2020/04/covid-19-water-what-can-we-learn/ (Accessed: 17 September 2024).
2. Zulfiqar M., Samsudin M. F. R., and Sufian S., "Modelling and optimization of photocatalytic degradation of phenol via TiO_2 nanoparticles: An insight into response surface methodology and artificial neural network," *J. Photochem. Photobiol. A Chem.*, **2019**, 384, 112039, doi: 10.1016/j.jphotochem.2019.112039.
3. Pavithra K. G., Kumar P. S., Jaikumar V., and Rajan P. S., "Removal of colorants from wastewater : A review on sources and treatment strategies," *J. Ind. Eng. Chem.*, **2019**, 75, 1–19, doi: 10.1016/j.jiec.2019.02.011.
4. Vanhulle, S., Trovaslet, M., Enaud, E., Lucas, M., Taghavi, S., Van der Lelie, D., Van Aken, B., Foret, M., Onderwater, R. C. A., Wesenberg, D., Agathos, S. N., Schneider, Y.-J., and Corbisier, A.-M., "Genotoxicity Reduction During a Combined Ozonation / Fungal Treatment of Dye-Contaminated Wastewater," *Env. Sci Technol*, **2008**, 42, 584–589, doi: 10.1021/es071300k.
5. Das T. R., Patra S., Madhuri R., and Sharma P. K., "Bismuth oxide decorated graphene oxide nanocomposites synthesized via sonochemical assisted hydrothermal method for adsorption of cationic organic dyes," *J. Colloid Interface Sci.*, **2018**, 509, 82–93, doi: 10.1016/j.jcis.2017.08.102.
6. Hafiz M., Hassanein A., Talhami M., Al-Ejji M., Hassan M. K., and Hawari A. H., "Magnetic nanoparticles draw solution for forward osmosis: Current status and future challenges in wastewater treatment," *J. Environ. Chem. Eng.*, **2022**, 10(6), 108955, doi: 10.1016/j.jece.2022.108955.

 doi:10.20944/preprints202506.0280.v1

7. Aslan S. and Şirazi M., "Adsorption of Sulfonamide Antibiotic onto Activated Carbon Prepared from an Agro-industrial By-Product as Low-Cost Adsorbent: Equilibrium, Thermodynamic, and Kinetic Studies," *Water, Air, Soil Pollut.*, **2020**, 231(5), 222, doi: 10.1007/s11270-020-04576-0.
8. Omri A., Wali A., and Benzina M., "Adsorption of bentazon on activated carbon prepared from Lawsonia inermis wood: Equilibrium, kinetic and thermodynamic studies," *Arab. J. Chem.*, **2016**, 9, 1729–S1739, doi: 10.1016/j.arabjc.2012.04.047.
9. Rosal, R., Rodríguez, A., Perdigón-Melón, J. A., Petre, A., García-Calvo, E., Gómez, M. J., Agüera, A., and Fernández-Alba, A. R., "Occurrence of emerging pollutants in urban wastewater and their removal through biological treatment followed by ozonation," *Water Res.*, **2010**, 44(2), 578–588, doi: 10.1016/j.watres.2009.07.004.
10. Ali, T., Tripathi, P., Azam, A., Raza, W., Ahmed, A. S., Ahmed, A., and Muneer, M., "Photocatalytic performance of Fe-doped TiO_2 nanoparticles under visible-light irradiation," *Mater. Res. Express*, **2017**, 4(1), 15022, doi: 10.1088/2053-1591/aa576d.
11. Karthik, C., Swathi, N., Pandi Prabha, S., and Caroline, D. G., "Green synthesized rGO-AgNP hybrid nanocomposite – An effective antibacterial adsorbent for photocatalytic removal of DB-14 dye from aqueous solution," *J. Environ. Chem. Eng.*, **2020**, 8(1), 103577, doi: 10.1016/j.jece.2019.103577.
12. McMullan, G., Meehan, C., Conneely, A., Kirby, N., Robinson, T., Nigam, P., Banat, I. M., Marchant, R., and Smyth, W. F., "Microbial decolourisation and degradation of textile dyes," *Appl. Microbiol. Biotechnol.*, **2001**, 56(1–2), 81–87, doi: 10.1007/s002530000587.
13. Emamjomeh M. M. and Sivakumar M., "Review of pollutants removed by electrocoagulation and electrocoagulation/flotation processes," *J. Environ. Manage.*, **2009**, 90(5), 1663–1679, doi: 10.1016/j.jenvman.2008.12.011.
14. Martínez-Huitle C. A., Rodrigo M. A., Sirés I., and Scialdone O., "Single and Coupled Electrochemical Processes and Reactors for the Abatement of Organic Water Pollutants: A Critical Review," *Chem. Rev.*, **2015**, 115(24), 13362–13407, doi: 10.1021/acs.chemrev.5b00361.
15. Momina and Ahmad K., "Feasibility of the adsorption as a process for its large scale adoption across industries for the treatment of wastewater: Research gaps and economic assessment," *J. Clean. Prod.*, **2023**, 388, 136014, doi: 10.1016/j.jclepro.2023.136014.
16. Kim S.-H., Kim D.-S., Moradi H., Chang Y.-Y., and Yang J.-K., "Highly porous biobased graphene-like carbon adsorbent for dye removal: Preparation, adsorption mechanisms and optimization," *J. Environ. Chem. Eng.*, **2023**, 11(2), 109278, doi: 10.1016/j.jece.2023.109278.
17. Dhamorikar, V. G. Lade, P. V Kewalramani, and A. B. Bindwal, "Review on integrated advanced oxidation processes for water and wastewater treatment," *J. Ind. Eng. Chem.*, **2024**, 138, 104–122, doi: 10.1016/j.jiec.2024.04.037.
18. Sirés I., Brillas E., Oturan M. A., Rodrigo M. A., and Panizza M., "Electrochemical advanced oxidation processes: Today and tomorrow. A review," *Environ. Sci. Pollut. Res.*, **2014**, 21(14), 8336–8367, doi: 10.1007/s11356-014-2783-1.
19. Ahmed S., Rasul M. G., Brown R., and Hashib M. A., "Influence of parameters on the heterogeneous photocatalytic degradation of pesticides and phenolic contaminants in wastewater: A short review," *J. Environ. Manage.*, **2011**, 92(3), 311–330, doi: 10.1016/j.jenvman.2010.08.028.
20. Sun, B., Li, H., Li, X., Liu, X., Zhang, C., Xu, H., and Zhao, X. S.., "Degradation of Organic Dyes over Fenton-Like Cu_2O-Cu/C Catalysts," *Ind. Eng. Chem. Res.*, **2018**, 57(42), 14011–14021, doi: 10.1021/acs.iecr.8b02697.
21. Susanti Y. D.and Saleh R., "Efficient photo-, sono-, and sonophoto-fenton-like degradation of the organic pollutant methylene blue using a $BiFeO_3$/graphene composite," *IOP Conf. Ser. Mater. Sci. Eng.*, **2020**, 763(1), doi: 10.1088/1757-899X/763/1/012064.
22. Vaishnave P., Ameta G., Kumara A., Sharma S., and Ameta S. C., "Sono-photo-Fenton and photo-Fenton degradation of methylene blue: A comparative study," *J. Indian Chem. Soc.*, **2011**, 88(3), 397–403, doi:
23. Halfadji A., Naous M., Kharroubi K. N., Belmehdi F. E. Z., and Aoudia H., "Facile prepared Fe_3O_4 nanoparticles as a nano-catalyst on photo-fenton process to remediation of methylene blue dye from water: characterisation and optimization," *Glob. Nest J.*, **2024**, 26(1), 1–6, doi: 10.30955/gnj.005312.

 doi:10.20944/preprints202506.0280.v1

24. Zhu, Y., Zhu, R., Yan, L., Fu, H., Xi, Y., Zhou, H., Zhu, G., Zhu, J., and He, H., "Visible-light Ag/AgBr/ferrihydrite catalyst with enhanced heterogeneous photo-Fenton reactivity via electron transfer from Ag/AgBr to ferrihydrite," *Appl. Catal. B Environ.*, **2018**, 239, 280–289, doi: 10.1016/j.apcatb.2018.08.025.
25. Jiang, J., Gao, J., Li, T., Chen, Y., Wu, Q., Xie, T., Lin, Y., and Dong, S., "Visible-light-driven photo-Fenton reaction with α-Fe_2O_3/BiOI at near neutral pH: Boosted photogenerated charge separation, optimum operating parameters and mechanism insight," *J. Colloid Interface Sci.*, **2019**, 554, 531–543, doi: 10.1016/j.jcis.2019.07.038.
26. Ahmed Y., Yaakob Z., and Akhtar P., "Degradation and mineralization of methylene blue using a heterogeneous photo-Fenton catalyst under visible and solar light irradiation," *Catal. Sci. Technol.*, 2016, 6(4), 1222–1232, doi: 10.1039/c5cy01494h.
27. Wang, L., Zhou, C., Yuan, Y., Jin, Y., Liu, Y., Jiang, Z., Li, X., Dai, J., Zhang, Y., Siyal, A. A., Ao, W., Fu, J., and Qu, J., "Catalytic degradation of crystal violet and methyl orange in heterogeneous Fenton-like processes," *Chemosphere*, **2023**, 344, 140406, doi: 10.1016/j.chemosphere.2023.140406.
28. Tryba B., Piszcz M., Grzmil B., Pattek-Janczyk A., and Morawski A. W., "Photodecomposition of dyes on Fe-C-TiO_2 photocatalysts under UV radiation supported by photo-Fenton process," *J. Hazard. Mater.*, **2009**, 162(1), 111–119, doi: 10.1016/j.jhazmat.2008.05.057.
29. Liu S.-Q., Feng L.-R., Xu N., Chen Z.-G., and. Wang X.-M,, "Magnetic nickel ferrite as a heterogeneous photo-Fenton catalyst for the degradation of rhodamine B in the presence of oxalic acid," *Chem. Eng. J.*, **2012**, 203, 432–439, doi: 10.1016/j.cej.2012.07.071.
30. Diao Y., Yan Z., Guo M., and Wang X., "Magnetic multi-metal co-doped magnesium ferrite nanoparticles: An efficient visible light-assisted heterogeneous Fenton-like catalyst synthesized from saprolite laterite ore," *J. Hazard. Mater.*, **2018**, 344, 829–838, 10.1016/j.jhazmat.2017.11.029.
31. Anchieta, C. G., Severo, E. C., Rigo, C., Mazutti, M. A., Kuhn, R. C., Muller, E. I., Flores, E. M. M., Moreira, R. F. P. M., and Foletto, E. L.., "Rapid and facile preparation of zinc ferrite ($ZnFe_2O_4$) oxide by microwave-solvothermal technique and its catalytic activity in heterogeneous photo-Fenton reaction," *Mater. Chem. Phys.*, **2015**, 160, 141–147, doi: 10.1016/j.matchemphys.2015.04.016.
32. Firouzeh N., Paseban A., Ghorbanian M., Asadzadeh S. N., and Amani A., "Recyclable Nano-Magnetic $CoFe_2O4$: a Photo-Fenton Catalyst for Efficient Degradation of Reactive Blue 19," *Bionanoscience*, **2024**, 14(4), 4481–4492, doi: 10.1007/s12668-024-01316-0.
33. Fahad Almojil S., Ning J., and Ibrahim Almohana A., "Photo-Fenton process for degradation of methylene blue using copper ferrite@sepiolite clay," *Inorg. Chem. Commun.*, **2024**, 166, 12623, doi: 10.1016/j.inoche.2024.112623.
34. Qin, L., Wang, Z., Fu, Y., Lai, C., Liu, X., Li, B., Liu, S., Yi, H., Li, L., Zhang, M., Li, Z., Cao, W., and Niu, Q. "Gold nanoparticles-modified $MnFe_2O_4$ with synergistic catalysis for photo-Fenton degradation of tetracycline under neutral pH," *J. Hazard. Mater.*, **2021**, 414, 125448, doi: 10.1016/j.jhazmat.2021.125448.
35. Jadhav S. A., Somvanshi S. B., Khedkar M. V, Patade S. R., and Jadhav K. M., "Magneto-structural and photocatalytic behavior of mixed Ni–Zn nano-spinel ferrites: visible light-enabled active photodegradation of rhodamine B," *J. Mater. Sci. Mater. Electron.*, **2020**, 31(14), 11352–11365, doi: 10.1007/s10854-020-03684-1.
36. Mendonça M. H., Godinho M. I.,. Catarino M. A, da Silva Pereira M. I., and Costa F. M., "Preparation and characterisation of spinel oxide ferrites suitable for oxygen evolution anodes," *Solid State Sci.*, **2002**, 4(2), 175–182, doi: 10.1016/S1293-2558(01)01238-9.
37. Valente, F., Astolfi, L., Simoni, E., Danti, S., Franceschini, V., Chicca, M., and Martini, A. "Nanoparticle drug delivery systems for inner ear therapy: An overview," *J. Drug Deliv. Sci. Technol.*, **2017**, 39, 28–35, doi: 10.1016/j.jddst.2017.03.003.
38. Casbeer E., Sharma V. K., and. Li X. Z, "Synthesis and photocatalytic activity of ferrites under visible light: A review," *Sep. Purif. Technol.*, **2012**, 87, 1–14, doi: 10.1016/j.seppur.2011.11.034.
39. Zhou, L., Ji, L., Ma, P.-C., Shao, Y., Zhang, H., Gao, W., and Li, Y., "Development of carbon nanotubes/$CoFe_2O_4$ magnetic hybrid material for removal of tetrabromobisphenol A and Pb(II)," *J. Hazard. Mater.*, **2014**, 265, 104–114, doi: 10.1016/j.jhazmat.2013.11.058.

 doi:10.20944/preprints202506.0280.v1

40. Rooygar A. A.,. Mallah M. H, Abolghasemi H., and Safdari J., "New 'magmolecular' process for the separation of antimony(III) from aqueous solution," *J. Chem. Eng. Data*, **2014**, 59(11), 3545–3554, doi: 10.1021/je500462.
41. Goswami M. and Phukan P., "Enhanced adsorption of cationic dyes using sulfonic acid modified activated carbon," *J. Environ. Chem. Eng.*, **2017**, 5(4), 3508–3517, doi: 10.1016/j.jece.2017.07.016.
42. Zabihi M., Khorasheh F., and Shayegan J., "Supported copper and cobalt oxides on activated carbon for simultaneous oxidation of toluene and cyclohexane in air," *RSC Adv.*, **2015**, 5(7), 5107–5122, doi: 10.1039/c4ra14430a.
43. Bouriche R., Tazibet S., Boutillara Y., Melouki R., Benaliouche F., and Boucheffa Y., "Characterization of Titanium (IV) Oxide Nanoparticles Loaded onto Activated Carbon for the Adsorption of Nitrogen Oxides Produced from the Degradation of Nitrocellulose," *Anal. Lett.*, **2021**, 54(12), 1929–1942, doi: 10.1080/00032719.2020.1829637.
44. Qadri S., Ganoe A., and Haik Y., "Removal and recovery of acridine orange from solutions by use of magnetic nanoparticles," *J. Hazard. Mater.*, **2009**, 169(1–3), 318–323, doi: 10.1016/j.jhazmat.2009.03.103.
45. Vasileiadou A., Zoras S., and Iordanidis A., "Bioenergy production from olive oil mill solid wastes and their blends with lignite: thermal characterization, kinetics, thermodynamic analysis, and several scenarios for sustainable practices," *Biomass Convers. Biorefinery*, **2023**, 13(6), 5325–5338, doi: 10.1007/s13399-021-01518-6.
46. Andriantsiferana C., Mohamed E. F., and Delmas H., "Photocatalytic degradation of an azo-dye on TiO_2/activated carbon composite material," *Environ. Technol. (United Kingdom)*, **2014**, 35(3), 355–363, doi: 10.1080/09593330.2013.828094.
47. Yuan R., Guan R., Shen W., and Zheng J., "Photocatalytic degradation of methylene blue by a combination of TiO_2 and activated carbon fibers," *J. Colloid Interface Sci.*, **2005**, 282(1), 87–91, doi: 10.1016/j.jcis.2004.08.143.
48. Bukhari, S. N. U. S., Shah, A. A., Liu, W., Channa, I. A., Chandio, A. D., Chandio, I. A., and Ibupoto, Z. H., "Activated carbon based TiO_2 nanocomposites (TiO_2@AC) used simultaneous adsorption and photocatalytic oxidation for the efficient removal of Rhodamine-B (Rh–B)," *Ceram. Int.*, **2024**, 50(21), 41285–41298, doi: 10.1016/j.ceramint.2024.07.440.
49. Thirumoolan, D., Ragupathy, S., Renukadevi, S., Rajkumar, P., Rai, R. S., Saravana Kumar, R. M., Hasan, I., Durai, M., and Ahn, Y.-H. "Influence of nickel doping and cotton stalk activated carbon loading on structural, optical, and photocatalytic properties of zinc oxide nanoparticles," *J. Photochem. Photobiol. A Chem.*, **2024**, 448, 115300, doi: 10.1016/j.jphotochem.2023.115300.
50. Tabaja, N., Brouri, D., Casale, S., Zein, S., Jaafar, M., Selmane, M., Toufaily, J., Davidson, A., and Hamieh, T., "Use of SBA-15 silica grains for engineering mixtures of oxides CoFe and NiFe for Advanced Oxidation Reactions under visible and NIR," *Appl. Catal. B Environ.*, **2019**, 253, 69–378, doi: 10.1016/j.apcatb.2019.04.073.
51. Tabaja, N., Casale, S., Brouri, D., Davidson, A., Obeid, H., Toufaily, J., and Hamieh, T., "Quantum-dots containing Fe/SBA-15 silica as green catalysts for the selective photocatalytic oxidation of alcohol (methanol, under visible light)," *Comptes rendus-Chim.*, **2015**,18(3), 358–367, doi: 10.1016/j.crci.2015.01.010.
52. Imraish, A., Abu Thiab, T., Al-Awaida, W., Al-Ameer, H. J., Bustanji, Y., Hammad, H., Alsharif, M., ad Al-Hunaiti A., "In vitro anti-inflammatory and antioxidant activities of $ZnFe_2O_4$ and $CrFe_2O_4$ nanoparticles synthesized using Boswellia carteri resin," *J. Food Biochem.*, **2021**, 45(6), 1–14, doi: 10.1111/jfbc.13730.
53. Liu, Q.-X., Zhou, Y.-R., Wang, M., Zhang, Q., Ji, T., Chen, T.-Y., & Yu, D.-C., "Adsorption of methylene blue from aqueous solution onto viscose-based activated carbon fiber felts: Kinetics and equilibrium studies," *Adsorpt. Sci. Technol.*, **2019**, 37(3–4), 312–332, doi: 10.1177/0263617419827437.
54. Liu P., Huang Y., and Zhang X., "Enhanced electromagnetic absorption properties of reduced graphene oxide-polypyrrole with $NiFe_2O_4$ particles prepared with simple hydrothermal method," *Mater. Lett.*, **2014**, 120, 143–146, doi: 10.1016/j.matlet.2014.01.054.
55. Parishani M., Nadafan M., Dehghani Z., Malekfar R., and Khorrami G. H. H., "Optical and dielectric properties of $NiFe_2O_4$ nanoparticles under different synthesized temperature," *Results Phys.*, **2017**, 7, 3619–3623, doi: 10.1016/j.rinp.2017.09.049.

 doi:10.20944/preprints202506.0280.v1

56. Luadthong C., Itthibenchapong V., Viriya-Empikul N., Faungnawakij K., Pavasant P., and Tanthapanichakoon W., "Synthesis, structural characterization, and magnetic property of nanostructured ferrite spinel oxides (AFe_2O_4, A = Co, Ni and Zn)," *Mater. Chem. Phys.*, **2013**, 143(1), 203–208, doi: 10.1016/j.matchemphys.2013.08.052.
57. Doğan M., Sabaz P., Bïcïl Z., Koçer Kizilduman B., and Turhan Y., "Activated carbon synthesis from tangerine peel and its use in hydrogen storage," *J. Energy Inst.*, **2020**, 93(6), 2176–2185, doi: 10.1016/j.joei.2020.05.011.
58. Baikousi, M., Dimos, K., Bourlinos, A. B., Zbořil, R., Papadas, I., Deligiannakis, Y., and Karakassides, M. A., "Surface decoration of carbon nanosheets with amino-functionalized organosilica nanoparticles," *Appl. Surf. Sci.*, **2012**, 258(8), 3703–3709, doi: 10.1016/j.apsusc.2011.12.010.
59. Shendrik R., Kaneva E., Radomskaya T., Sharygin I., and Marfin A., "Relationships between the structural, vibrational, and optical properties of microporous cancrinite," *Crystals*, **2021**, 11(3), 1–19, doi: 10.3390/cryst11030280.
60. Makofane A., Motaung D. E., and Hintsho-Mbita N. C., "Photocatalytic degradation of methylene blue and sulfisoxazole from water using biosynthesized zinc ferrite nanoparticles," *Ceram. Int.*, **2021**, 47(16), 22615–22626, doi: 10.1016/j.ceramint.2021.04.274.
61. Yousif, M., Ibrahim, A. H., Al-Rawi, S. S., Majeed, A., Iqbal, M. A., Kashif, M., Abidin, Z. U., Arbaz, M., Ali, S., Hussain, S. A., Shahzadi, A., and Haider, M. T. "Visible light assisted photooxidative facile degradation of azo dyes in water using a green method," *RSC Adv.*, **2024**, 14(23), 16138–16149, doi: 10.1039/d4ra01202j.
62. Srivastava, M., Singh, J., Yashpal, M., Gupta, D. K., Mishra, R. K., Tripathi, S., and Ojha, A. K.., "Synthesis of superparamagnetic bare Fe_3O_4 nanostructures and core/shell (Fe_3O_4/alginate) nanocomposites," *Carbohydr. Polym.*, **2012**, 89(3), 821–829, doi: 10.1016/j.carbpol.2012.04.016.
63. Sriramulu M., Shukla D., and Sumathi S., "Aegle marmelos leaves extract mediated synthesis of zinc ferrite: Antibacterial activity and drug delivery," *Mater. Res. Express*, **2018**, 5(11), 1–9, doi: 10.1088/2053-1591/aadd88.
64. Bharathi K. K., Noor-A-Alam M., Vemuri R. S., and Ramana C. V., "Correlation between microstructure, electrical and optical properties of nanocrystalline NiFe1.925Dy 0.075O_4 thin films," *RSC Adv.*, **2012**,2(3), 941–948, doi: 10.1039/c1ra00161b.
65. Aladdin Jasim N., Esmail Ebrahim S., and Ammar S. H., "Fabrication of $Zn_xMn_{1-x}Fe_2O_4$ metal ferrites for boosted photocatalytic degradation of Rhodamine-B dye," *Results Opt.*, **2023**, 13, 00508, doi:.1016/j.rio.2023.100508.
66. Toor A. T., Verma A.,. Jotshi C. K, Bajpai P. K., and Singh V., "Photocatalytic degradation of Direct Yellow 12 dye using UV/TiO_2 in a shallow pond slurry reactor," *Dye. Pigment.*, **2006**, 68(1), 53–60, doi: 10.1016/j.dyepig.2004.12.009.
67. Panda N., Sahoo H., and Mohapatra S., "Decolourization of Methyl Orange using Fenton-like mesoporous Fe_2O_3-SiO_2 composite," *J. Hazard. Mater.*, **2011**,185(1), 359–365, doi: 10.1016/j.jhazmat.2010.09.042.
68. Sedlak D. L., "Factors Affecting the Yield of Oxidants from the Reaction of Nanoparticulate Zero-Valent Iron and Oxygen," *Environ. Sci. Technol.*, **2008**, 42(4), 1262–1267, doi: 10.1021/es7025664.
69. Yu L., Chen J., Liang Z., Xu W., Chen L., and Ye D., "Degradation of phenol using Fe_3O_4-GO nanocomposite as a heterogeneous photo-Fenton catalyst," *Sep. Purif. Technol.*, **2016**, 171, 80–87, doi: 10.1016/j.seppur.2016.07.020.
70. Lu J., Xing J., Chen D., Xu H., Han X., and Li D., "Enhanced photocatalytic activity of β-Ga_2O_3 nanowires by Au nanoparticles decoration," *J. Mater. Sci.*, **2019**, 54(8), 6530–6541, doi: 10.1007/s10853-019-03359-1.